

# Identification campaign of supernova remnant candidates in the Milky Way – I: Chandra observation of G308.3-1.4

C. Y. Hui<sup>1</sup>, K. A. Seo<sup>1</sup>, R. H. H. Huang<sup>2</sup>, L. Trepl<sup>3</sup>, Y. J. Woo<sup>1</sup>, T.-N. Lu<sup>2</sup>, A. K. H. Kong<sup>2,4</sup>, and F. M. Walter<sup>5</sup>

## ABSTRACT

ROSAT all-sky survey (RASS) data have provided another window to search for supernova remnants (SNRs). In reexamining this data archive, a list of unidentified extended X-ray objects have been suggested as promising SNR candidate. However, most of these targets have not yet been fully explored by the state-of-art X-ray observatories. For selecting a pilot target for a long-term identification campaign, we have observed the brightest candidate, G308.3-1.4, with Chandra X-ray observatory. An incomplete shell-like X-ray structure which well-correlated with the radio shell emission at 843 MHz has been revealed. The X-ray spectrum suggests the presence of a shock-heated plasma. All these evidences confirm G308.3-1.4 as a SNR. The brightest X-ray point source detected in this field-of-view is also the one locates closest to the geometrical center of G308.3-1.4, which has a soft spectrum. The intriguing temporal variability and the identification of optical/infrared counterpart rule out the possibility of an isolated neutron star. On the other hand, the spectral energy distribution from  $K_s$  band to  $R$  band suggests a late-type star. Together with a putative periodicity of  $\sim 1.4$  hrs, the interesting excesses in  $V$ ,  $B$  bands and  $H\alpha$  suggest this source as a promising candidate of a compact binary survived in a supernova explosion (SN).

*Subject headings:* supernova remnants — X-rays: individual (G308.3-1.4)

## 1. INTRODUCTION

Most Galactic SNRs were identified by radio observations (Green 2009). However, one should notice that there are various selection effects in the Galactic surveys for SNRs in the radio band. For example, Schaudel (2003) suggested that Galactic SNRs older than  $\sim 5 \times 10^4$  yrs are difficult to be detected with the current radio telescopes due to their low surface brightness. Therefore, the currently known SNR population of our Galaxy is certainly biased.

There are 274 SNRs have been uncovered in the Milky Way so far (Green 2009). This known sample is far smaller than the expected population. Assuming a typical evolution timescale of SNRs before they merge with the ISM ( $\sim 10^5$  yrs) and a event rate of 2 SNe/century in the Milky Way (Dragicovich et al. 1999),  $\sim 2000$  SNRs are expected in our Galaxy. Such a great deficit again

points to the selection effects in the past surveys.

Besides radio observations, the ROSAT all-sky survey (RASS) provides us with an alternative window for searching SNRs in our Galaxy. Schaudel (2003) suggests that the energy band (0.1–2.4 keV) of the Positional Sensitive Proportional Counter (PSPC) on board ROSAT allows the detection of SNRs for an interstellar absorption  $\leq 3 \times 10^{22} \text{ cm}^{-2}$ . A simulation of the theoretical distribution of SNe and their remnants in the Galactic plane has predicted somewhat more than 200 SNRs should possibly be detected in RASS (Busser 1998). In examining the RASS database, Schaudel (2003) has reported  $\sim 100$  unidentified extended X-ray sources as the possible SNR candidates.

Although the RASS database allows one to search for SNR candidates, the short exposure of few hundred seconds and the poor spatial resolution in survey mode ( $\sim 96''$ ) prevent any firm

identification of their nature. In addition, a possible hard X-ray ( $> 2$  keV) component could arise from the interactions of the reflected shocks with the dense ambient medium or alternatively from the synchrotron emission radiated by the relativistic leptons. However, the limited energy bandwidth of ROSAT does not allow one to determine whether an additional component presents in the hard X-ray band. In view of its much improved spatial resolution and the enlarged effective area, Chandra X-ray Observatory and XMM-Newton Observatory provide the most suitable instruments to clarify the emission nature of these candidates. And this motivates an extensive identification campaign of all these unidentified extended RASS objects with the state-of-art X-ray telescopes.

For an initial stage of the campaign, we chose the brightest SNR candidate in the list provided by Schaudel (2003), G308.3-1.4, as the pilot target. G308.3-1.4 was firstly listed as a possible SNR candidate in the MOST SNR catalogue based on its radio morphology and the spectral index (Whiteoak 1992). In the RASS image, G308.3-1.4 shows centrally-peaked X-ray emission with a diameter of  $\sim 10'$  which coincides with a radio arc-like feature (see Figure 1). The radio contours obtained from the 843 MHz Sydney University Molonglo Sky Survey (**SUMSS**) data (Bock et al. 1999). However, owing to the poor spatial resolution of RASS data, it is unclear whether the X-rays are originated from the radio shell structure. Also, the limited photon statistic of G308.3-1.4 in the RASS data do not allow any further probe of its emission properties. In this paper, we report the first detailed investigation for the nature of G308.3-1.4 with Chandra observation.

## 2. OBSERVATIONS

G308.3-1.4 was observed with Chandra in 2010 June 26 – 27 with the Advanced CCD Imaging Spectrometer (ACIS) using a frame time of 3.2 s. Since the source extent cannot be accurately determined from the RASS data, we utilized the whole ACIS-I CCD array with an intention to cover the whole feature with aimpoint at the nominal center of the extended RASS feature (i.e. RA= $13^{\text{h}}40^{\text{m}}56.3^{\text{s}}$  Dec= $-63^{\circ}43'32.6''$  (J2000)). For data reduction as well as analysis, we utilized

the Chandra Interactive Analysis of Observations software (CIAO 4.3) throughout this study. We have firstly reprocessed the data with CALDB (ver. 4.4.3) to correct for an error in the time-dependent gain correction (TGAIN) during the observation by using the script *chandra\_repro*. To facilitate a source detection with high positional accuracy, we have applied the subpixel event repositioning in reprocessing the data. The effective exposure of this observation is  $\sim 14.9$  ks. We restricted all the analysis in an energy band of  $0.5 - 8$  keV.

We have also conducted a series of Target-of-Opportunity (ToO) observations of this source with the Ultra-Violet and Optical Telescope (UVOT) onboard the SWIFT satellite. The pre-processed calibrated science grade (level II) data were used. This pre-processing includes bad pixel correction and the reduction of the modulo 8 fixed-pattern which results from the fact that raw image pixel are smaller by up to factor of 8 than the original detector pixels. In addition, the images have been flatfield corrected. The data were then analyzed by using the HEASoft Swift package.

## 3. SPATIAL ANALYSIS

An X-ray color image of the ACIS-I data of G308.3-1.4 is displayed in Figure 2. With the superior spatial resolution of Chandra, an incomplete X-ray shell structure have been revealed. We have overlaid the same SUMSS radio contours (cf. Fig. 1) onto Figure 2. This comparison demonstrates a clear correlation between the X-ray emission and the radio feature, and hence their connection is confirmed unambiguously and suggest G308.3-1.4 belongs to category of mixed-morphology SNRs. The incomplete X-ray shell-like morphology conforms with a circle with an angular radius of  $\theta \sim 5'$  approximately centered at RA= $13^{\text{h}}41^{\text{m}}32^{\text{s}}$  Dec= $-63^{\circ}42'44''$  (J2000).

Figure 2 also shows the hardness distribution of the X-rays from G308.3-1.4. Several components can be identified in this color image. Apart from the bright outer rim emission, a fainter but harder feature is noticed in its inner edge which we refer as the “inner rim” in this paper. Besides these two shell-like components, soft and fainter diffuse emission is found in the region close to the center.

This observation also enable a search for X-ray

point sources in the vicinity of G308.3-1.4. By means of a wavelet source detection algorithm, 17 sources has been detected in the field-of-view. These sources are labeled in Figure 3. The source positions, positional errors, net count rates, signal-to-noise ratios as well as the estimates of spatial extent of all these sources are given in Table 1. The brightest object is the source marked as #7 in Figure 3, which is also the one located closest the geometrical center. Cross-correlating these sources with the SIMBAD and NED databases did not result in any identification within a search radius of 5 arcsec around each source.

To investigate if these sources are promising isolated neutron star candidates we proceeded to search for their possible optical counterparts by utilizing the USNO-B1.0 catalogue (Monet et al. 2003). The X-ray-to-optical flux ratio,  $f_x/f_{\text{opt}}$ , provides a rudimentary parameter for discriminating the source nature. For an isolated neutron star,  $f_x/f_{\text{opt}}$  is typically larger than 1000 (cf. Haberl 2007). On the other hand,  $f_x/f_{\text{opt}}$  for the field stars and the active galactic nuclei are much lower which typically  $< 0.3$  and  $< 50$  respectively (Maccacaro et al. 1988; Stocke et al. 1991). We have systematically searched for the optical counterparts within a  $10\sigma \times 10\sigma$  error box centered at each X-ray position. Among all 17 sources, only the object labeled as #5 have no optical counterpart found in its error box. For those 16 X-ray objects have optical counterparts identified, we have calculated the X-ray-to-optical flux ratios with the  $B$ -band magnitudes from the USNO-B1.0 catalogue. The X-ray fluxes  $f_x$  of these objects are estimated from the net count rates in Table 1 with the aid of *PIMMS* (ver. 4.3) by assuming a power-law spectrum with a photon index of 2. The flux ratio of source #7,  $f_x/f_B \sim 1.5$  is found to be the highest among all these 16 sources. For source #5, despite no optical counterpart have been identified in this search, the limiting magnitude of USNO-B1.0 catalogue (i.e.  $\sim 21$ ) results in a lower limit of  $f_x/f_B \gtrsim 3$  which is not tight enough to constrain its source nature. Furthermore, its X-ray spectral properties do not conform with that of a neutron star (see §5). Therefore, we conclude that we do not find any concrete evidence for an isolated neutron star in this investigation.

Besides radio and X-ray data, we have also explored the infrared data obtained by **Wide-field**

**Infrared Survey Explorer** (WISE; Wright et al. 2010). In Figure 4, we compared the  $22 \mu\text{m}$  image with the same set of radio contours used in Figure 1 and Figure 2. An extended incomplete elliptical feature has been identified in this mid-infrared image. This feature has a semi-major/semi-minor axis of  $\sim 10'/8'$  with the major axis oriented  $\sim 20^\circ$  from north. On the southwestern edge of this feature, an infrared rim emission is found to be well-correlated with the radio shell and the outer-rim X-ray emission of G308.3-1.4 (cf. Figure 2). This strongly suggests that these rim structures seen in different wavelengths are intrinsically related.

Apart from this rim, there appears to be a cavity in the southwestern quarter of this infrared feature (Fig. 4). This is the region where the X-ray emission is most prominent (see Fig. 2 and Fig. 3). We also noticed that the incomplete radio shell apparently complements the peripheral of the incomplete elliptical infrared structure. Also, there is no X-ray/radio emission toward the northeastern region where the infrared feature is bright. Such morphology resembles those of the SNRs which have interactions with the surrounding cloud complex (e.g. Sasaki et al. 2004). However, as there is no reliable distance estimates for the X-ray/radio and the infrared features, the physical association between the large infrared structure and the X-ray/radio shell remains uncertain. Further investigations for this possible shock-cloud interaction, such as maser observations (see Wardle & Yusef-Zadeh 2002), are encouraged.

#### 4. TEMPORAL ANALYSIS

We have also examined the temporal behavior of these two relatively bright sources with reasonable photon statistics. With the aid of the tool *axbary*, their arrival times were firstly barycentric-corrected by using the corresponding X-ray positions reported in Table 1. With the aid of the tool *glvary*, we searched for variability by using the Gregory-Loredo algorithm (Gregory & Loredo 1992). For source #5, a zero variability index has been assigned and the probability of variable signal is found to be  $\sim 11\%$ .<sup>6</sup> And hence, no evidence of variability is found for this source. On the other hand, a variability index of 8 is assigned for

<sup>6</sup><http://cxc.harvard.edu/ciao/threads/variable/index.html#output>

source #7 and the probability of variable signal is at the level  $> 99.99\%$ , which strongly suggests the presence of temporal variability. We have cross-checked these results by adopting other statistical tests (e.g.  $\chi^2$  test), which resulted in the same conclusion as aforementioned.

Figure 5 shows the light curve of source #7 with a binned time of 1000 s. Burst-like activity is noticed in the beginning of this observation (i.e. 2<sup>nd</sup> bin of Fig.5). However, the limited photon statistics does not allow a firm conclusion to be drawn. Except for this, the light curve appears to be rather steady. After excluding the time segment possibly contains the flare, we proceeded to search for the possible periodic signals from source #7. By fitting the light curve with a sinusoidal, we have identified an interesting periodicity candidate at  $P = 1.4 \pm 0.2$  hrs. The epoch-folded light curve is shown in Figure 6.  $\chi^2$  test indicates that it is different from a uniform distribution at 99.97% confidence level. While the periodic variation appears to be promising, we stress that the peak-to-peak modulation is only at a marginal level of  $\sim 4\sigma$  due to the large error bars. A deeper observation is required to confirm this interesting periodicity candidate. On the other hand, we do not find any promising periodic signal from source #5 in this observation.

## 5. SPECTRAL ANALYSIS

For the spectral analysis, we extracted the spectra for various components of G308.3-1.4 from the regions illustrated in Figure 7. These regions are carefully selected so that they are free from the contamination of the point spread function (PSF) wing from any resolved source. The background spectra for the corresponding CCD chips were extracted from the source free regions.

We utilized the tool *specextract* to extract the spectra and to compute the response files. After background subtraction, there are net counts of  $5118 \pm 73$  cts (outer rim),  $1302 \pm 37$  cts (inner rim) and  $1157 \pm 36$  cts (central region) available for analysis. According to the photon statistics, we group each of the extracted spectrum dynamically so as to achieve a comparable signal-to-noise ratio. The energy spectra of different components are displayed in Figure 8. Emission lines from various metals can be clearly observed (e.g. Mg at

$\sim 1.4$  keV; Si at  $\sim 1.9$  keV), which support the SNR nature of G308.3-1.4.

We examined these spectra with an absorbed non-equilibrium ionization model of a constant temperature and a single ionization timescale (XSPEC model: NEI). All the spectral fittings were performed with XSPEC 12.6.0. The best-fit parameters are summarized in Table 2. All quoted errors are  $1\sigma$  for 1 parameter of interest. For all three investigated regions, we do not find any conclusive evidence for the deviation of metal abundances from the solar values.

The ionization timescale inferred from fitting the outer rim spectrum and the inner rim spectrum is  $\tau_{\text{ion}} = (7.3 \pm 1.5) \times 10^{10}$  s  $\text{cm}^{-3}$  and  $\tau_{\text{ion}} = (4.3^{+2.1}_{-1.2}) \times 10^{10}$  s  $\text{cm}^{-3}$  respectively, which indicate these parts of the remnant might not yet reach the collisional ionization equilibrium (CIE). The best-fit plasma temperature of outer rim and inner rim are found to be  $kT = 0.63^{+0.05}_{-0.02}$  keV and  $kT = 0.97^{+0.19}_{-0.16}$  keV respectively. The higher temperature at the inner rim is consistent with the hardness distribution shown in the color image (i.e. Fig. 2). The moderate temperature variation can possibly be caused by the complex density structure in the shocked region (e.g. see Chevalier 1982).

For the spectrum of the central region, the ionization timescale cannot be properly constrained in NEI model fitting. We put a lower bound of  $\tau_{\text{ion}}$  at  $\gtrsim 10^{13}$  s  $\text{cm}^{-3}$ . This suggests the central region can possibly reach the condition for CIE already. The best-fit plasma temperature of this region is found to be  $kT = 0.57 \pm 0.03$  keV.

We further investigated if there is any non-thermal emission in various regions by adding a power-law model on the aforementioned best-fit plasma models. We found that the parameters of the additional power-law cannot be properly constrained. This prompts us to perform the spectral fit with the photon index fixed at the value of  $\Gamma = 2$ . For all three spectra, no significant improvement of the goodness-of-fit have been found. We place  $1\sigma$  upper limits of any non-thermal emission at the levels of  $< 1.9 \times 10^{-14}$  erg  $\text{cm}^{-2}$   $\text{s}^{-1}$ ,  $< 3.5 \times 10^{-14}$  erg  $\text{cm}^{-2}$   $\text{s}^{-1}$  and  $< 4.5 \times 10^{-14}$  erg  $\text{cm}^{-2}$   $\text{s}^{-1}$  for the outer rim, inner rim and the central region respectively.

We have also examined the spectrum for the

brightest source detected in the FOV (i.e. source #7). The source spectrum has been extracted from a circular region with a radius of  $5''$  centered at the position reported by the source detection algorithm (cf. Tab 1). For the background subtraction, we sampled from an annulus centered on the same position with an inner/outer radius of  $7''/14''$ . There are  $156 \pm 13$  net counts available for the spectral fitting.

We have firstly examined the spectrum with various single component models, including the blackbody, the power-law and the hot diffuse gas model based on Mewe et al. (1985) (XSPEC model: MEKAL). We found all the tested single component model cannot provide any adequate description of the data. All result in a reduced  $\chi^2$  (i.e.  $\chi^2/\text{d.o.f.}$ ) larger than 2 which indicate these models do not provide an adequate description of the data. We proceeded to perform the fitting with double blackbody which generally describes the spectrum of a particular manifestation of neutron stars, namely the central compact objects (CCOs) (Hui 2007; Mereghetti 2011).

A double blackbody fit yields  $N_H = (1.5 \pm 0.7) \times 10^{22} \text{ cm}^{-2}$ ,  $kT_1 = 0.09_{-0.02}^{+0.04} \text{ keV}$ ,  $kT_2 = 0.44_{-0.10}^{+0.21} \text{ keV}$  with an acceptable goodness-of-fit  $\chi^2=7.3$  for 5 d.o.f.. Their normalizations imply the emitting regions with the radii of  $R_1 = 27_{-21}^{+30} D_{\text{kpc}} \text{ km}$  and  $R_2 = 35_{-18}^{+34} D_{\text{kpc}} \text{ m}$ , where  $D_{\text{kpc}}$  is the source distance in unit of kpc. The unabsorbed flux of source #7 is found to be  $f_x \simeq 1.3 \times 10^{-11} \text{ erg cm}^{-2} \text{ s}^{-1}$  in 0.5-8 keV. The comparison between this best-fit model and the observed data is displayed in Figure 9.

We have also examined the spectrum of source #7 with a blackbody plus power-law model, which is a typical phenomenological description for the spectrum of a quiescent low-mass X-ray binary. This model yields  $N_H = (1.5_{-0.7}^{+1.2}) \times 10^{22} \text{ cm}^{-2}$ ,  $kT = 0.09_{-0.03}^{+0.02} \text{ keV}$ ,  $R_{\text{bb}} = 24_{-10}^{+23} D_{\text{kpc}} \text{ km}$ ,  $\Gamma = 2.3_{-0.2}^{+0.7}$  and the power-law normalization of  $(6.0_{-2.8}^{+4.7}) \times 10^{-5} \text{ photons keV}^{-1} \text{ cm}^{-2} \text{ s}^{-1}$  at 1 keV. The goodness-of-fit ( $\chi^2=8.0$  for 5 d.o.f.) is comparable with that resulted from the double blackbody fit. The unabsorbed flux in 0.5-8 keV inferred from this model is  $f_x \simeq 1.1 \times 10^{-11} \text{ erg cm}^{-2} \text{ s}^{-1}$ .

For source#5, the second brightest objects detected in the FOV without any optical counterpart

identified, the source spectrum and the adopted background are extracted from the regions with the same sizes in the case of source #7 but centered at the nominal position of source#5 (Tab 1). After background subtraction, there are  $61 \pm 8$  cts available for the analysis. Among the tested single component model, we found that MEKAL provides a better description for the spectrum of this object ( $\chi^2=1.4$  for 3 d.o.f.) than a blackbody ( $\chi^2=21.1$  for 3 d.o.f.) or a power-law ( $\chi^2=4.8$  for 3 d.o.f.). The best-fit model yields  $N_H = (5.7_{-1.9}^{+2.9}) \times 10^{21} \text{ cm}^{-2}$  and  $kT = 0.46_{-0.26}^{+0.16} \text{ keV}$ . This infers an unabsorbed flux of  $f_x \simeq 2.0 \times 10^{-13} \text{ erg cm}^{-2} \text{ s}^{-1}$  in 0.5-8 keV.

## 6. OPTICAL/INFRARED SPECTRAL ENERGY DISTRIBUTION OF THE CENTRAL COMPACT OBJECT

We have also examined the optical properties for the counterpart of source #7. In USNO-B1.0 catalog, only a single source with the magnitudes of  $B = 19.72$ ,  $R = 19.64$  and  $I = 16.15$  has been identified within its  $10\sigma \times 10\sigma$  X-ray error box. We have also searched for the infrared counterpart in the Two Micron All Sky Survey (2MASS) catalog (Skrutskie et al. 2006). Similarly, only one source with  $J = 14.01$ ,  $H = 13.31$ , and  $K_s = 13.10$  can be found with its error box. To complement these catalog values, we have also carried out observations in  $V$  and  $U$  band so as to have a more complete frequency coverage.

For  $U$  band, by applying aperture photometry to the stacked UVOT image with an exposure of 6.49 ks, we have placed an limiting magnitude of 21.29. The UVOT data also allow us to cross-check the magnitude in  $B$  band, from which we have obtained  $B=19.77$  which confirms the value reported in USNO-B1.0 catalog. For  $V$ -band, we have observed source #7 with the Cerro Tololo Interamerican Observatory (CTIO). Data have been obtained using the ANDICAM dual-channel imaging photometer at the SMARTS/CTIO 1.3 m telescope in  $V$  filter. The zero-point corrected magnitude is found to be  $V = 19.16$ .

These identifications enable us to construct an optical/infrared spectral energy distribution (SED) which is shown in Figure 10. We adopted the column density inferred the X-ray spectral fit of source #7 (i.e.  $1.5 \times 10^{22} \text{ cm}^{-2}$ ) to perform

the extinction-correction (cf. Predehl & Schmitt 1995; Cardelli, Clayton, & Mathis 1989). The dereddened SED has also been plotted in Figure 10. For the range from  $K_s$  band to  $R$  band, the SED can be modeled with the spectrum of a M3V star. On the other hand, an apparent excess is found at and beyond  $V$  band.

To further constrain its optical properties, we have also searched for its  $H\alpha$  counterpart from the SuperCOSMOS H-alpha Survey (SHS) catalog (Parker et al. 2005). Within the X-ray error box of source #7, only one source with the magnitude 17.35 is found. In comparison with  $R$  band,  $m_{H\alpha} - m_R = -2.3$ , a clear enhancement in  $H\alpha$  is noted which suggests the presence of a strong emission line.

## 7. DISCUSSION

We have performed a detailed spectro-imaging X-ray study of the SNR candidate G308.3-1.4 with Chandra. An incomplete shell-like X-ray structure, which is well-correlated with radio shell, has been revealed. Its X-ray spectrum has shown the presence of a hot plasma accompanied with metallic emission lines. All these observational evidences clearly suggest G308.3-1.4 is indeed a SNR.

Utilizing the X-ray results, we proceed to discuss the properties of G308.3-1.4. The emission measure inferred from the spectral fits of the outer rim emission allows us to estimate the hydrogen density  $n_H$  and the electron density  $n_e$  in the shocked regions. Assuming the shocked densities of hydrogen and electrons are uniform in the extraction region, the normalization of the NEI model can be approximated by  $10^{-14} n_H n_e V / 4\pi D^2$ , where  $D$  is the distance to G308.3-1.4 in cm and  $V$  is the volume of interest in units of  $\text{cm}^3$ . Assuming a geometry of oblated spheroid, the volume of interest for the outer rim is  $5 \times 10^{54} D_{\text{kpc}}^3 \text{cm}^3$  where  $D_{\text{kpc}}$  is the remnant distance in units of kpc. Assuming a fully ionized plasma with  $\sim 10\%$  He ( $n_e \sim 1.2n_H$ ), the  $1\sigma$  confidence interval of the outer rim normalization implies the shocked hydrogen and electron densities in the ranges of  $n_H \simeq (2.8 - 3.2) D_{\text{kpc}}^{-0.5} \text{cm}^{-3}$  and  $n_e \simeq (3.3 - 3.9) D_{\text{kpc}}^{-0.5} \text{cm}^{-3}$  respectively.

Assuming G308.3-1.4 is in a Sedov phase, the shock temperature can be estimated by  $T_s \simeq 8.1 \times 10^6 E_{51}^{2/5} n_{\text{ISM}-1}^{-2/5} t_4^{-6/5} \text{K}$ , where  $t_4$ ,  $E_{51}$  and

$n_{\text{ISM}-1}$  are the time after the explosion in units of  $10^4$  years, the released kinetic energy in units of  $10^{51}$  ergs and the ISM density of  $0.1 \text{cm}^{-3}$  respectively. Assuming it is a strong shock,  $n_{\text{ISM}}$  is estimated as  $0.25n_H$ . Taking the  $1\sigma$  uncertainties of the temperature and the normalization for the outer rim into account (cf. Tab. 2), the age of G308.3-1.4 is constrained in the brackets of  $t \simeq (2.4 - 2.7) D_{\text{kpc}}^{1/6} \times 10^3 \text{yrs}$  and  $t \simeq (5.1 - 5.9) D_{\text{kpc}}^{1/6} \times 10^3 \text{yrs}$  for  $E_{51} = 0.1$  and  $E_{51} = 1$  respectively. Since the distance plays a crucial role in determining the physical properties of G308.3-1.4, a follow-up HI observation of G308.3-1.4 is strongly recommended.

Our observation has also revealed a number of sources in the field of G308.3-1.4 (cf. Fig. 3). Source #7 is the most interesting source in this population. First, among all the detected sources, it is the closest object from the geometric center of the remnant with an offset of  $\sim 1.4'$ . Also, the column absorption of this object inferred from the spectral fit is not far from the value inferred from the remnant spectrum, which suggests a possible tie between source #7 and G308.3-1.4. Its spectrum can be described by a composite blackbody or a blackbody plus power-law model, though the parameters are rather unconstrained due to the small photon statistic resulted from this short exposure. We would like to point out that these properties are similar to those of CCOs, which is one of the most poorly known classes among all known manifestations of neutron stars (see Mereghetti 2011 for a recent review). CCOs are typically characterized by their proximity to the expansion center of the associated SNRs as well as their thermal X-ray spectra (Mereghetti 2011; Hui 2007).

On the other hand, all the known CCOs are also characterized by their large X-ray-to-optical flux ratios ( $f_x/f_{\text{opt}} > 10^3$ ) which is typical for isolated neutron stars (cf. De Luca 2008). In searching for the counterpart of source #7, we have identified a single optical/infrared source within the error box of source #7, which clearly rules out the possibility of an isolated neutron star.

However, we cannot exclude the possibility that this is a neutron star resides in a binary system that survived in the SN explosion. The binary scenario is also suggested by the putative modulation

of  $P \sim 1.4$  hrs, which can possibly be the orbital period of this system. A similar scenario has also been suggested to explain the X-ray temporal behavior of the peculiar CCO associated with the SNR RCW 103 which has a periodic modulation at 6.67 hrs that can also be interpreted as the orbital period (Pizzolato et al. 2008; De Luca et al. 2006). Nevertheless, this relatively short exposure in our observation do not provide a firm conclusion on the periodicity of source #7. A longer follow-up X-ray observation can enable us to better constrain its temporal behavior.

Similar to the CCO in RCW 103, flux variability has also been detected from source #7 in G308.3-1.4 (see Fig. 5). The nature of this variability remains unknown. Speculations have been ranged from the instability of the accretion disc around the compact object to the scenario that the CCO is a magnetar (De Luca et al. 2006). The X-ray source in RCW 103 is so far the only CCO that has demonstrated long-term flux variability. It is possible that source #7 in G308.3-1.4 can be the second example. Multi-epoch X-ray monitoring of this source can provide a deeper insight on its temporal behavior.

The properties of the infrared/optical counterpart of source #7 are also worth discussing. We found that its SED can be well-described by the model spectrum of a late-type star in the range from  $K_s$  band to  $R$  band (see Fig. 10). In the context of a binary scenario, this suggests the evidence for the companion star of source #7. Nevertheless, with these sparse data points obtained from the catalogs, its nature cannot be constrained unambiguously. Dedicated spectroscopic observations are required to provide us a deeper insight of it.

The other interesting optical properties are the enhancements observed in  $V$ ,  $B$  bands as well as  $H\alpha$ . These characteristics suggest the presence of an accretion disk around a compact object and a low mass companion (e.g. Cool et al. 1998). However, these excesses are larger than those observed from a typical quiescent low-mass x-ray binary (e.g. Haggard et al. 2004). As the orbital period of source #7 is suggested to be  $\sim 1.4$  hrs, it is expected to be a very compact binary system. Such tight orbit can possibly lead to the aforementioned large enhancements. Confirmation of this putative orbital period can provide a natural

explanation of the optical properties.

We would like to highlight that there are only 11 CCOs have been uncovered so far (cf. Tab. 1 in Mereghetti 2011). With this limited sample size, we cannot even determine if these objects consist of a homogeneous class. For a better understanding of their nature, the sample of CCOs has to be enlarged. In this aspect, our long-term X-ray identification campaign of SNR candidates can also enable the search for the candidates of these compact objects.

## 8. SUMMARY

There is a group of unidentified extended RASS objects have been suggested as promising SNR candidates. We have initiated a long-term identification campaign by observing the brightest candidate, G308.3-1.4, with Chandra. With a short exposure, we have confirmed the nature of G308.3-1.4 as a SNR through a detailed X-ray spectro-imaging analysis. Apart from the remnant emission, a bright X-ray point source locates close to the geometrical center of G308.3-1.4 has also been detected as a new CCO. This compact object has shown a putative periodicity of  $\sim 1.4$  hrs and excesses in  $V$ ,  $B$  bands and  $H\alpha$ , which suggest it as a promising candidate of a compact binary survived in a SN. In conclusion, this proposed alternative window of SNRs and compact objects survey has been demonstrated to be fruitful by our pilot target.

The authors would like to thank the anonymous referee for the useful comments. CYH is supported by the National Research Foundation of Korea through grant 2011-0023383. LT would like to thank the German Deutsche Forschungsgemeinschaft, DFG for financial support in project SFB TR 7 Gravitational Wave Astronomy. AKHK is supported partly by the National Science Council of the Republic of China (Taiwan) through grant NSC99-2112-M-007-004-MY3 and a Kenda Foundation Golden Jade Fellowship.

## REFERENCES

- Bock, D., M.I. Large, M.I., & Sadler, E.M. 1999, *AJ*, 117, 1578
- Busser, J. U. Z. 1998, PhD thesis, Munich Uni.

- Cardelli, J. A., Clayton, G. C., & Mathis, J. S. 1989, *ApJ*, 345, 245
- Chevalier, R. A. 1982, *ApJ*, 258, 790
- Cool, A. M., Grindlay, J. E., Cohn, H. N., Lugger, P. M., & Bailyn, C. D. 1998, *ApJ*, 508, L75
- De Luca, A. 2008, 40 YEARS OF PULSARS: Millisecond Pulsars, Magnetars and More. AIP Conference Proceedings, Volume 983, pp. 311-319 (2008)
- De Luca, A., Caraveo, P. A., Mereghetti, S., Tiengo, A., & Bignami, G. F. 2006, *Science*, 313, 814
- Dragicevich, P. M., Blair, D. G., & Burman, R. R. 1999, *MNRAS*, 302, 693
- Haberl, F. 2007, *Ap&SS*, 308, 181
- Haggard, D., et al. 2004, *ApJ*, 613, 512
- Hui, C. Y. 2007, PhD thesis, Ludwig-Maximilians Universität München
- Green D.A., 2009, 'A Catalogue of Galactic Supernova Remnants (2009 March version)', Mullard Radio Astronomy Observatory, Cavendish Laboratory, Cambridge, United Kingdom
- Gregory, P. C., & Loredo, T. J. 1992, *ApJ*, 398, 146
- Maccararo, T., Gioia, I. M., Wolter, A., Zamorani, G., & Stocke, J. T. 1988, *ApJ*, 326, 680
- Mereghetti, S. 2011, High-Energy Emission from Pulsars and their Systems, *Astrophysics and Space Science Proceedings*, ISBN 978-3-642-17250-2. Springer-Verlag Berlin Heidelberg, 2011, p. 345
- Mewe, R., Gronenschild, E.H.B.M., & van den Oord, G.H.J. 1985, *A&AS*, 62, 197
- Monet, D., et al. 2003, *AJ*, 125, 984
- Parker, Q. A., et al. 2005, *MNRAS*, 362, 689
- Pickles, A. J. 1998, *PASP*, 110, 863
- Pizzolato, F., Colpi, M., De Luca, A., Mereghetti, S., & Tiengo, A. 2008, *ApJ*, 681, 530
- Predehl, P., & Schmitt, J.H.M.M. 1995, *A&A*, 293, 889
- Sasaki, M., et al. 2004, *ApJ*, 617, 322
- Schaudel, D. 2003, PhD thesis, Ludwig-Maximilians Universität München
- Skrutskie, M. F., et al. 2006, *AJ*, 131, 1163
- Stocke, J. T., et al. 1991, *ApJS*, 76, 813
- Wardle, M., & Yusef-Zadeh, F. 2002, *Science*, 296, 2350
- Whiteoak, J. B. Z. 1992, *A&A*, 262, 251
- Wright, E. L., et al. 2010, *AJ*, 140, 1868

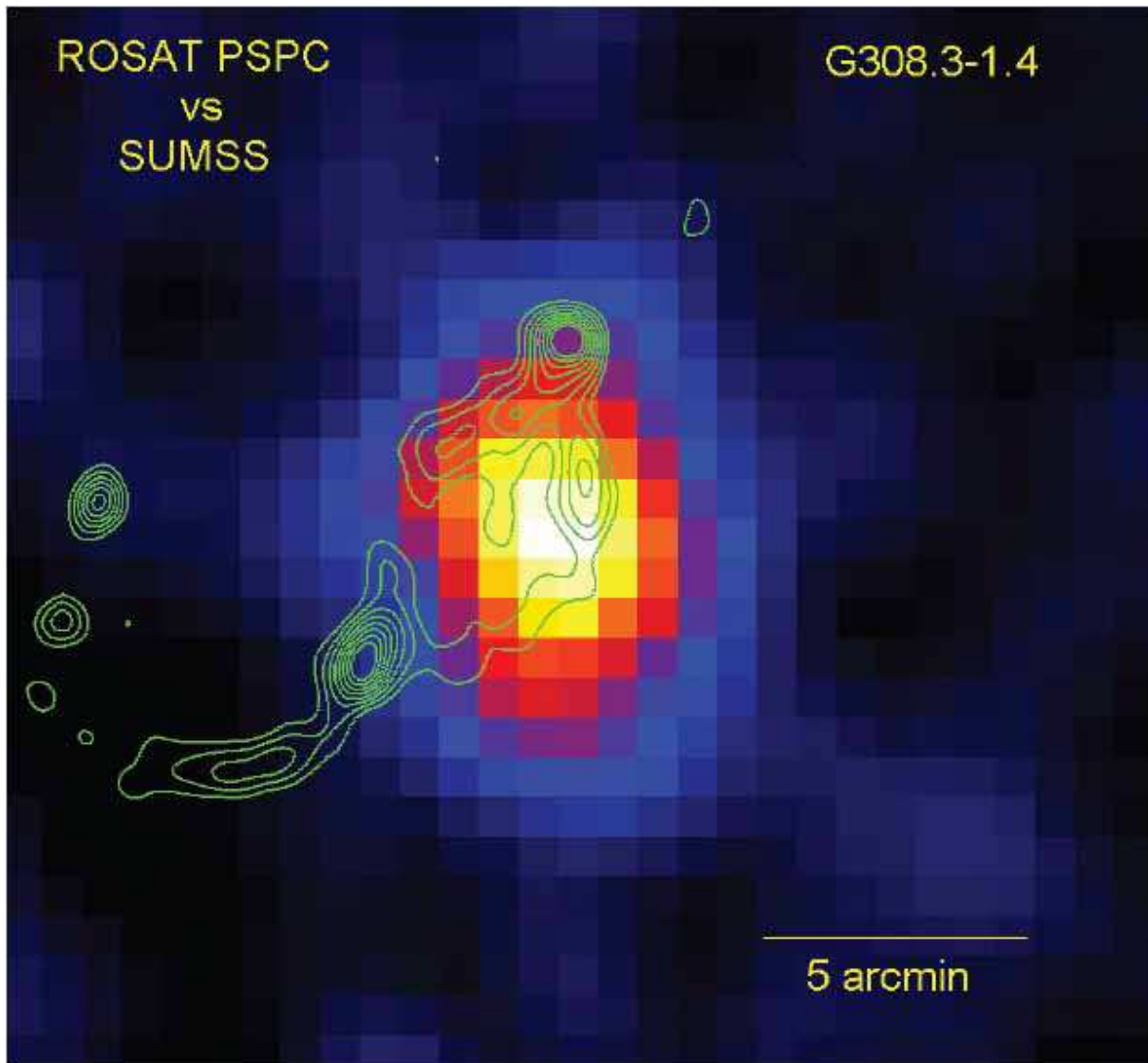


Fig. 1.— ROSAT PSPC image of G308.3-1.4 in the energy band of 0.1 – 2.4 keV with radio contour lines at the levels of 5 – 30 mJy/beam from the SUMSS data overlaid. Top is north and left is east.

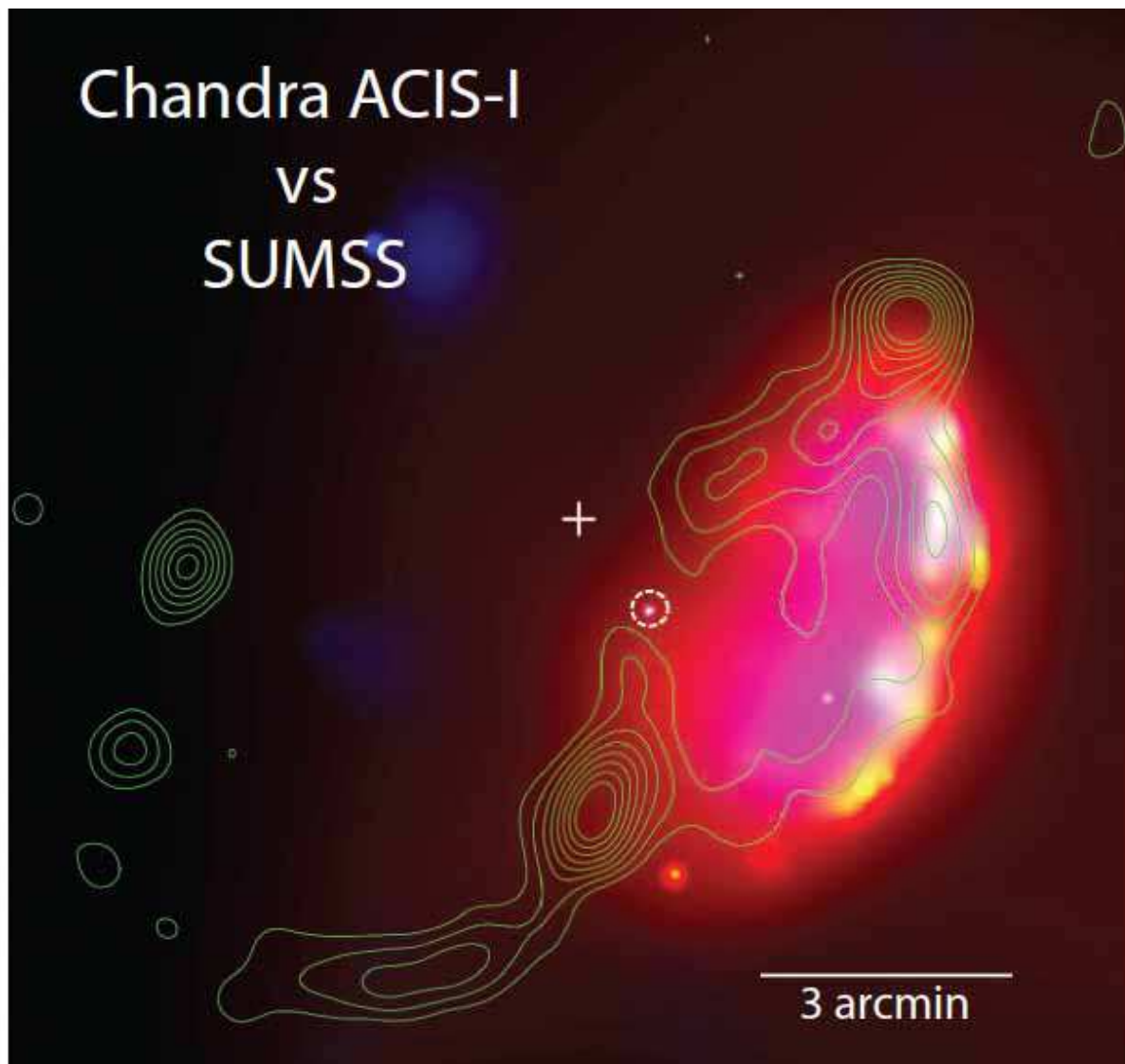


Fig. 2.—  $10' \times 10'$  Chandra ACIS-I X-ray colour image of G308.3-1.4 (red: 0.5 – 1 keV, green: 1 – 2 keV, blue: 2 – 8 keV). The binning factor of this image is  $2''$ . Adaptive smoothing has been applied to achieve a minimum signal-to-noise ratio of 3. The same radio contour lines as in Fig. 1 are overlaid for comparison. The geometrical center inferred from the X-ray morphology is illustrated by the cross. A bright source which locates closest to the geometrical center (i.e. source#7 in Fig. 3 and Tab. 1) is highlighted by the dash circle. Top is north and left is east.

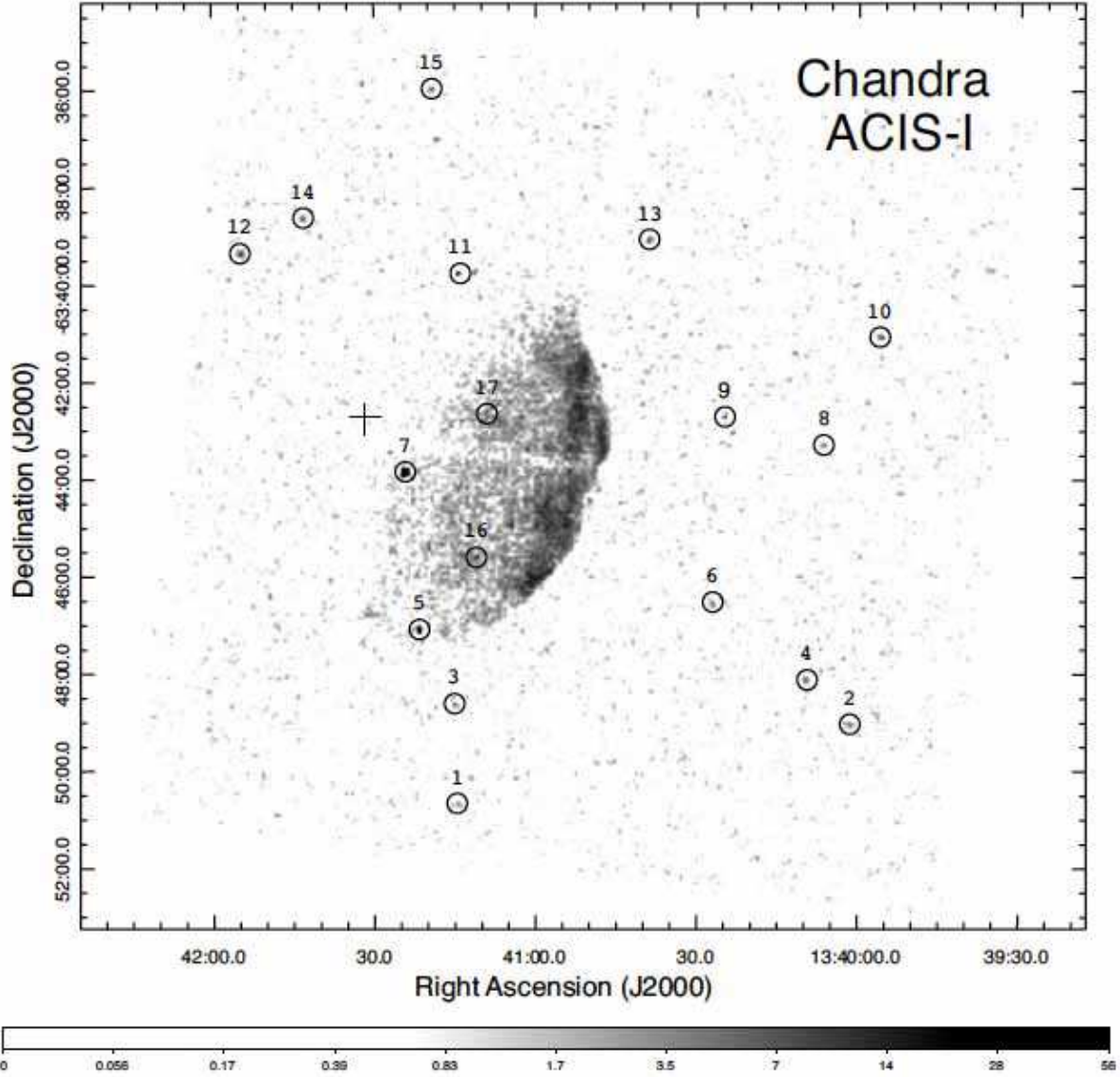


Fig. 3.— 17 X-ray sources detected in the whole ACIS-I image of G308.3-1.4 by wavelet detection algorithm. The properties of these source are summarized in Tab. 1. The geometrical center inferred from the X-ray morphology is illustrated by the cross.

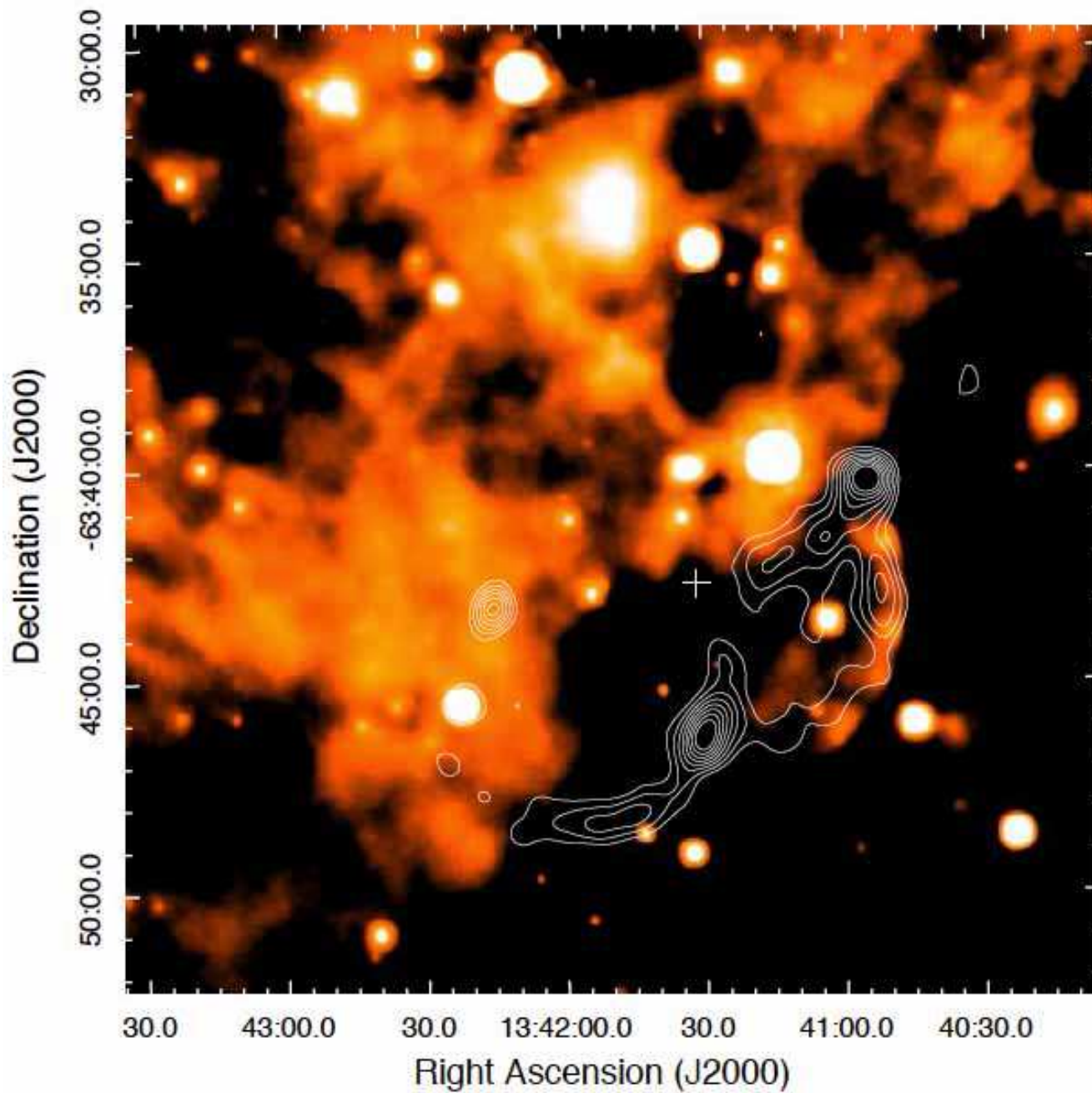


Fig. 4.— The  $22\ \mu\text{m}$  image of the  $23' \times 23'$  field around G308.3-1.4 as observed by WISE. The same radio contour lines as in Fig. 1 and Fig.2 are overlaid for comparison. The geometrical center inferred from the X-ray morphology is illustrated by the cross.

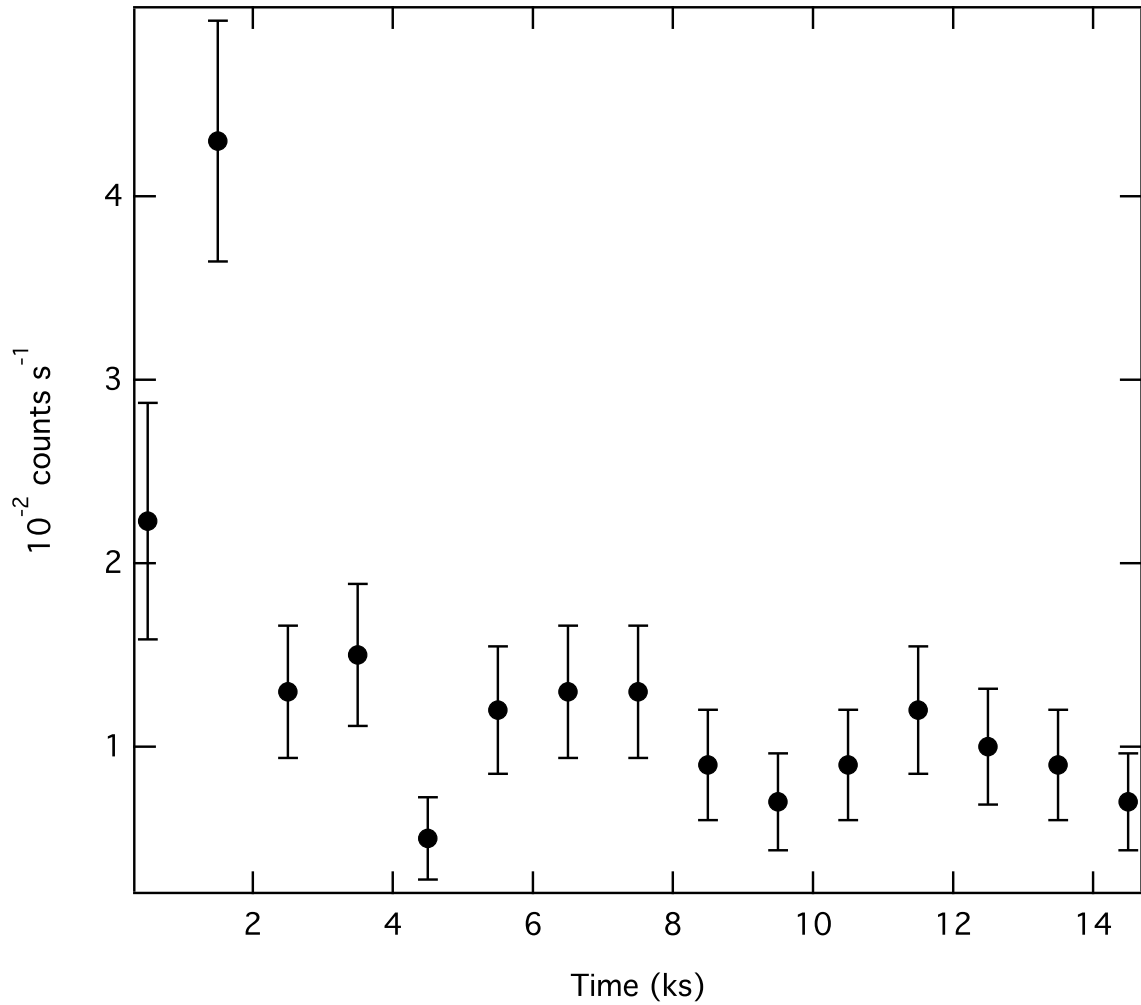


Fig. 5.— The light curve of the X-ray source #7 detected by Chandra ACIS-I which has shown its variability during the observation. The error bars represent  $1\sigma$  uncertainties.

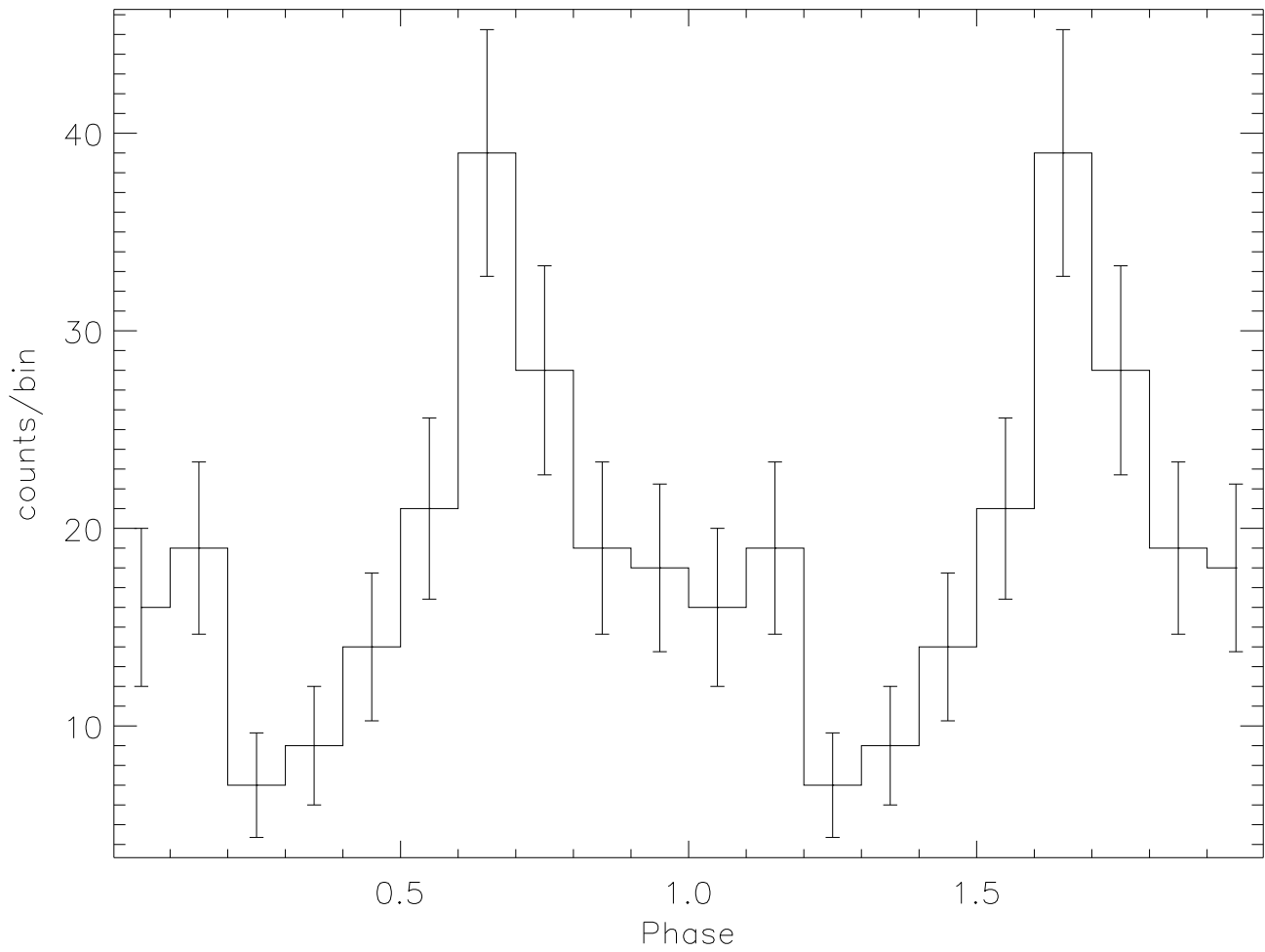


Fig. 6.— X-ray counts of source #7 versus phase for a periodicity candidate of 1.4 hrs. Two periodic cycles are shown for clarity. The error bars represent  $1\sigma$  uncertainties.

Table 1: Positions of the X-ray sources detected in the field of ACIS-I as labeled in Fig. 3. The corresponding  $1\sigma$  positional errors, net count rates, signal-to-noise ratios as well as the estimates of source extent are tabulated.

Source	RA (J2000)	Dec (J2000)	$\delta$ RA	$\delta$ Dec	Net count rate	S/N <sup>a</sup>	PSF RATIO <sup>b</sup>
	h:m:s	d:m:s	arcsec	arcsec	$10^{-3}$ cts s <sup>-1</sup>	$\sigma_G$	
1	13:41:15.00	-63:50:41.65	2.97	0.82	0.85±0.31	3.13	2.26
2	13:40:01.41	-63:49:04.98	2.81	1.25	1.45±0.40	4.38	2.64
3	13:41:15.06	-63:48:37.41	2.74	0.82	0.92±0.34	3.06	4.19
4	13:40:10.00	-63:48:10.30	2.05	1.45	1.29±0.40	3.76	3.74
5	13:41:22.00	-63:47:05.85	0.25	0.19	6.47±0.78	13.31	1.64
6	13:40:27.00	-63:46:31.78	2.78	1.03	1.15±0.36	3.77	7.13
7	13:41:24.00	-63:43:52.40	0.37	0.19	12.96±1.03	26.20	5.25
8	13:40:06.00	-63:43:20.13	2.15	1.32	0.71±0.28	2.87	3.19
9	13:40:24.57	-63:42:40.36	2.03	1.45	1.32±0.38	4.25	10.30
10	13:39:56.00	-63:41:04.22	1.77	0.77	1.46±0.42	4.24	1.96
11	13:41:14.29	-63:39:46.21	2.01	0.46	1.61±0.38	6.00	4.53
12	13:41:55.00	-63:39:21.22	1.18	0.68	2.14±0.45	6.74	1.46
13	13:40:38.82	-63:39:04.23	1.13	0.68	1.95±0.47	5.32	3.04
14	13:41:42.44	-63:38:36.12	3.08	1.01	1.19±0.37	3.71	3.46
15	13:41:19.00	-63:35:55.49	2.87	1.11	1.06±0.36	3.40	2.41
16	13:41:11.00	-63:45:39.36	1.23	0.56	2.45±0.73	3.63	12.21
17	13:41:08.98	-63:42:39.32	0.96	0.55	3.19±0.89	3.84	11.03

<sup>a</sup> Estimates of source significance in units of Gehrels error:  $\sigma_G = 1 + \sqrt{C_B + 0.75}$  where  $C_B$  is the background counts.

<sup>b</sup> The ratios between the source extents and the estimates of the PSF sizes.

Table 2: X-ray spectral parameters inferred from different regions in G308.3-1.4.

	Outer rim	Inner rim	Central region
$N_H$ ( $10^{21}$ cm <sup>-2</sup> )	10.3 <sup>+0.3</sup> <sub>-0.4</sub>	9.7 <sup>+0.8</sup> <sub>-0.7</sub>	9.4 <sup>+0.3</sup> <sub>-0.4</sub>
$kT$ (keV)	0.63 <sup>+0.05</sup> <sub>-0.02</sub>	0.97 <sup>+0.19</sup> <sub>-0.16</sub>	0.57 ± 0.03
$\tau_{\text{ion}}$ (s cm <sup>-3</sup> )	$(7.3 \pm 1.5) \times 10^{10}$	$(4.3^{+2.1}_{-1.2}) \times 10^{10}$	$> 10^{13}$
Norm ( $10^{-3}$ ) <sup>a</sup>	4.5 <sup>+0.6</sup> <sub>-0.7</sub>	0.5 <sup>+0.2</sup> <sub>-0.1</sub>	0.9 ± 0.1
$f_x$ ( $10^{-12}$ erg cm <sup>-2</sup> s <sup>-1</sup> ) <sup>b</sup>	24.1 <sup>+3.1</sup> <sub>-3.4</sub>	3.8 <sup>+1.1</sup> <sub>-0.9</sub>	2.3 <sup>+0.4</sup> <sub>-0.3</sub>
$\chi^2$	157.08	141.49	131.94
D.O.F.	138	129	122

<sup>a</sup> The model normalization is expressed as  $(10^{-14}/4\pi D^2) \int n_e n_H dV$  where  $D$  is the source distance in cm and  $n_e$  and  $n_H$  are the post-shock electron and hydrogen densities in cm<sup>-3</sup>.

<sup>b</sup> Unabsorbed flux over the energy range of 0.5 – 8 keV.

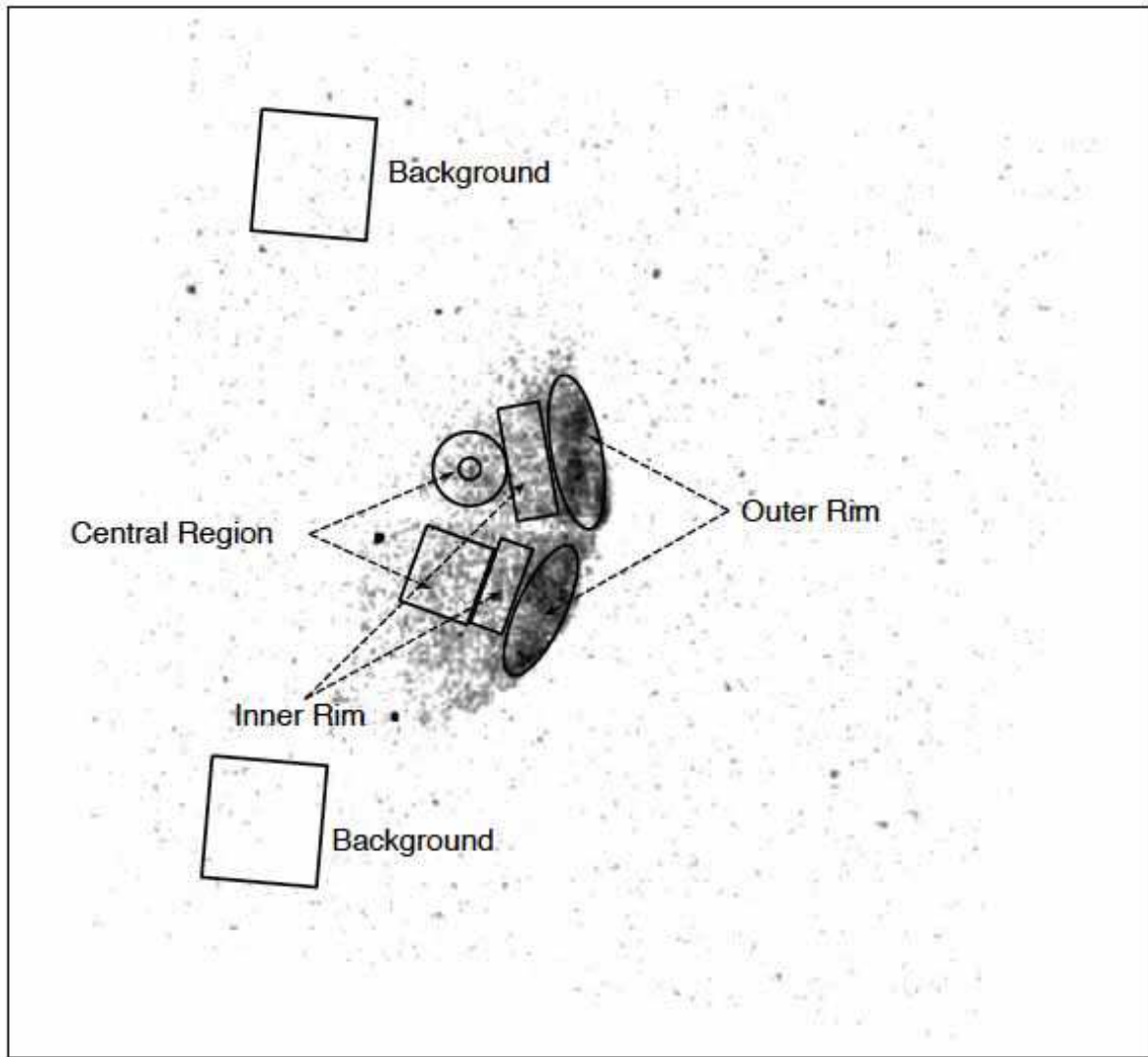


Fig. 7.— Illustration of the regions used to extract the spectra from different parts of G308.3-1.4.

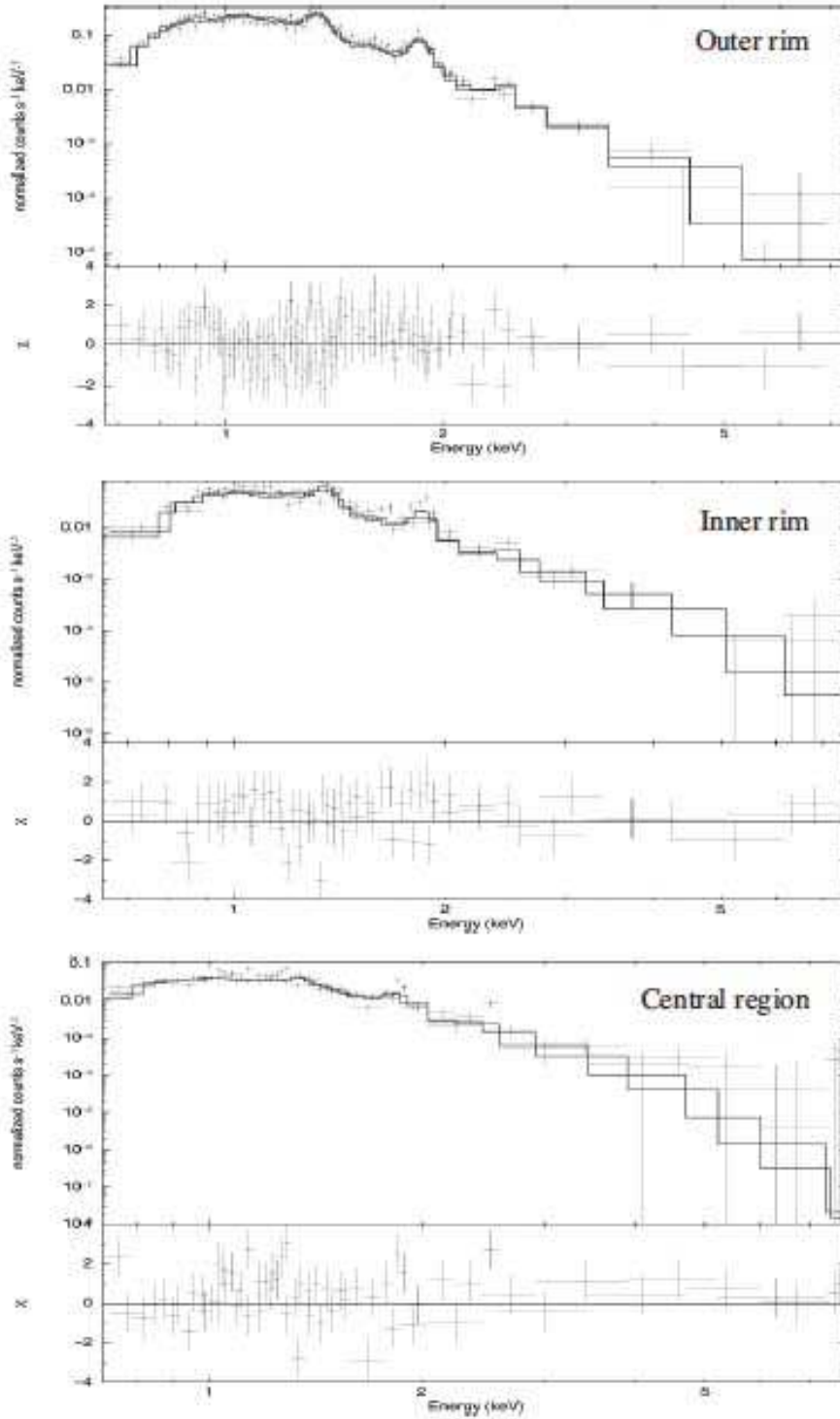


Fig. 8.— X-ray spectra of the emission from various regions of G308.3-1.4 as observed by Chandra ACIS-I. Residuals resulted from fitting an absorbed non-equilibrium ionization plasma model are shown for each cases. The error bars represent  $1\sigma$  uncertainties.

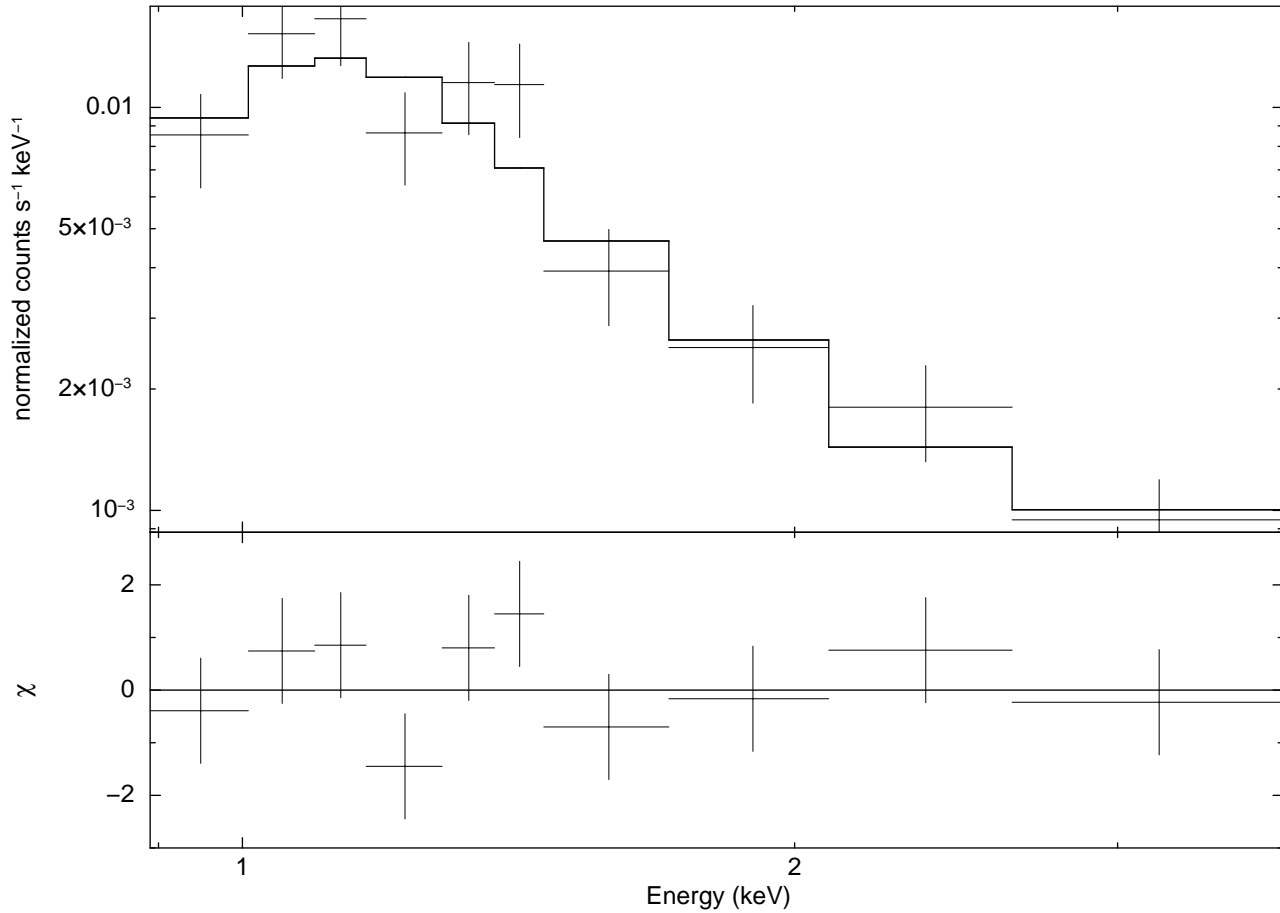


Fig. 9.— X-ray spectrum of the emission from the position of source #7 as observed with ACIS-I with the best-fit double blackbody model (*upper panel*) and contributions to the  $\chi^2$  statistics (*lower panel*). The error bars represent  $1\sigma$  uncertainties.

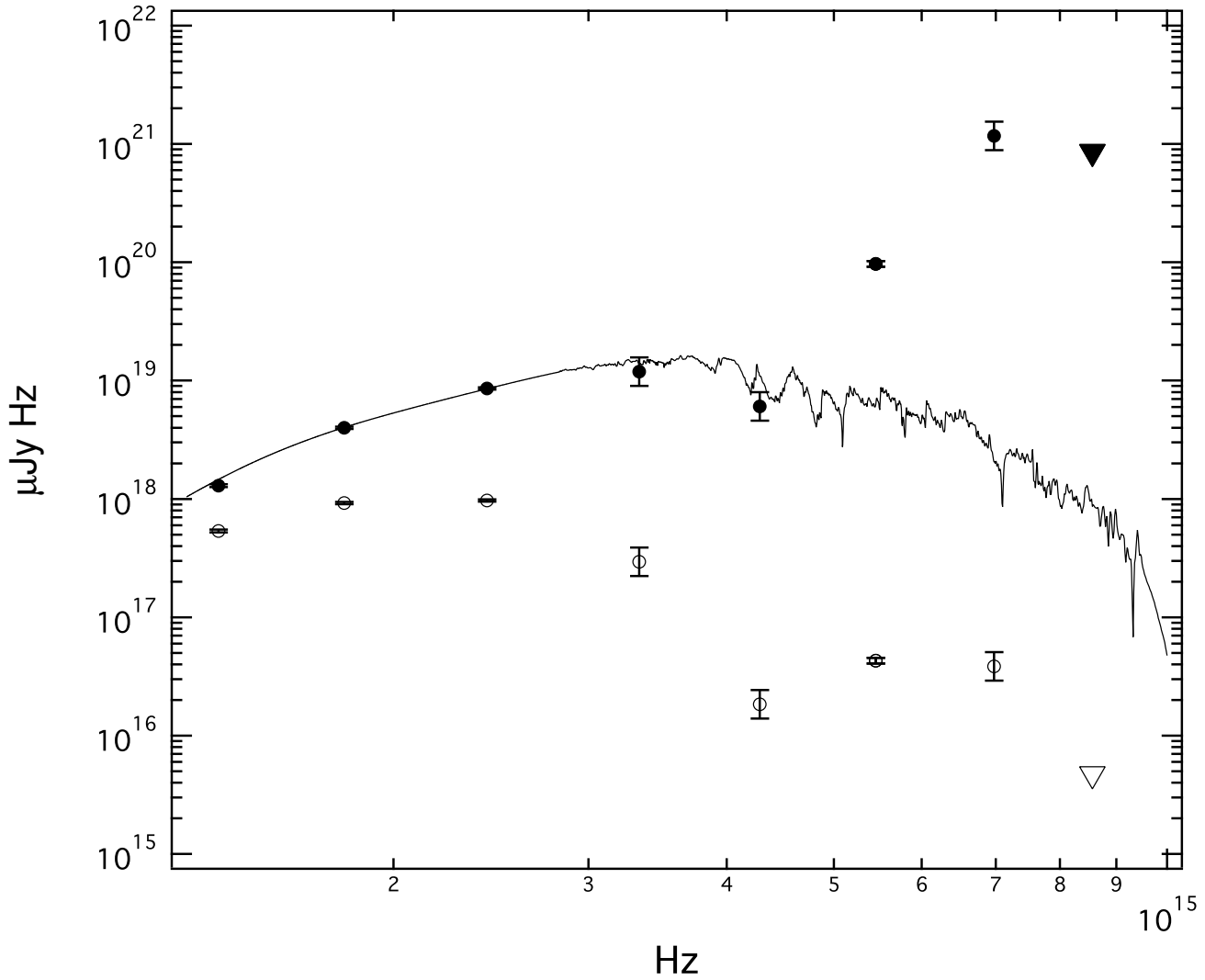


Fig. 10.— Optical/infrared spectral energy distribution of source #7. Both observed (open symbols) and de-reddened (solid symbols) data points are shown in this plot. The open and solid triangles represent the observed and de-reddened  $3\sigma$  upper limit inferred from SWIFT UVOT observation. The spectral model of a M3V star obtained from the stellar spectral flux library (Pickles 1998) is overplotted. The error bars represent the photometric uncertainties corresponding to each data point.